Modeling Stellar Collisions in Galactic Nuclei Using Hydrodynamic Simulations and Machine Learning

Sanaea C. Rose , James C. Lombardi, Jr. , Elena González Prieto , Fulya Kiroğlu , and Frederic A. Rasio .

¹Center for Interdisciplinary Exploration and Research in Astrophysics (CIERA) and Department of Physics and Astronomy, Northwestern University, 2145 Sheridan Road, Evanston, IL 60201, USA

²Department of Physics, Allegheny College, Meadville, Pennsylvania 16335, USA

ABSTRACT

Nuclear star clusters represent some of the most extreme collisional environments in the Universe. A typical nuclear star cluster harbors a supermassive black hole at its center, which accelerates stars to high speeds ($\gtrsim 100\text{-}1000 \text{ km/s}$) in a region where millions of other stars reside. Direct collisions occur frequently in such high-density environments, where they can shape the stellar populations and drive the evolution of the cluster. We present a suite of a couple hundred high-resolution smoothed-particle hydrodynamics (SPH) simulations of collisions between 1 M_{\odot} stars, at impact speeds representative of galactic nuclei. We use our SPH dataset to develop physically-motivated fitting formulae for predicting collision outcomes. While collision-driven mass loss has been examined in detail in the literature, we present a new framework for understanding the effects of "hit-and-run" collisions on a star's trajectory. We demonstrate that the change in stellar velocity follows the tidal-dissipation limit for grazing encounters, while the deflection angle is well-approximated by point-particle dynamics for periapses ≥ 0.3 times the stellar radii. We use our SPH dataset to test two machine learning (ML) algorithms, k-Nearest Neighbors and neural networks, for predicting collision outcomes and properties. We find that the neural network out-performs k-Nearest Neighbors and delivers results on par with and in some cases exceeding the accuracy of our fitting formulae. We conclude that both fitting formulae and ML have merits for modeling collisions in dense stellar environments, however ML may prove more effective as the parameter space of initial conditions expands.

Keywords: Stellar dynamics (1596), Star clusters (1567), Galactic center (565), Hydrodynamics (1963), Stellar mergers (2157)

1. INTRODUCTION

Supermassive black holes (SMBH) are ubiquitous at the centers of galaxies and are often surrounded by dense stellar clusters (e.g., Ferrarese & Ford 2005; Ghez et al. 2005; Neumayer et al. 2020; Schödel et al. 2003; Gallego-Cano et al. 2018). These dense environments facilitate frequent close encounters between stars, including direct collisions (e.g., Bailey & Davies 1999; Rauch 1999; Dale & Davies 2006; Dale et al. 2009; Davies et al. 2011; Rubin & Loeb 2011; Mastrobuono-Battisti et al. 2021; Rose et al. 2023). One characteristic that sets nuclear star clusters apart from other collisional stellar systems, such as globular clusters, is that the SMBH dominates the gravitational potential in the inner ~ 1 pc. Globular clusters have low velocity dispersions, and collisions there often result in stellar mergers (e.g., Lombardi et al. 1996, 2002; González et al. 2021; Rodriguez et al. 2022).

The SMBH, in contrast, accelerates stars on close-in orbits ($\lesssim 0.1~\rm pc$) to high speeds (e.g., Alexander 1999; Ghez et al. 2005; Genzel et al. 2003, 2010a). As a result, the impact speeds of colliding stars range from hundreds to thousands of km/s (e.g., Rauch 1999; Rose et al. 2023). The most energetic collisions can drive significant mass loss from the stars, in some cases completely destroying them (e.g., Lai et al. 1993; Freitag & Benz 2005; Balberg et al. 2013; Gibson et al. 2025; Ryu et al. 2024; Dessart et al. 2024; Brutman et al. 2024).

Collisions have a number of implications for the stellar populations in galactic nuclei, astrophysical transients, and bulk properties of the cluster. For example, destructive collisions near the SMBH may be associated with transients both from the collisions themselves and from interactions of the ejected stellar material with the SMBH (e.g., Balberg et al. 2013; Amaro Seoane 2023;

Ryu et al. 2024; Dessart et al. 2024; Brutman et al. 2024). Destructive collisions have also long been recognized as an important channel for shaping the stellar density profile in the inner region of a nuclear star cluster (e.g., Duncan & Shapiro 1983; Murphy et al. 1991; David et al. 1987a,b; Rauch 1999; Freitag & Benz 2002; Rose & MacLeod 2024; Balberg 2024; Ashkenazy & Balberg 2024). Furthermore, high-speed collisions and the peculiar stripped stars they produce have been connected to SMBH transients like tidal disruption events (Gibson et al. 2025; Rose & Mockler 2025).

The large range of speeds characteristic of galactic nuclei translates to diverse collision outcomes within the stellar population, depending on where the collision occurs in the cluster. While destructive collisions dominate in the inner ~ 0.01 pc, further from the SMBH, the velocity dispersion is lower and collisions can result in mergers (e.g., Mastrobuono-Battisti et al. 2021; Rose et al. 2023). These collisions can give rise to blue stragglers (e.g., Lombardi et al. 1996, 2002; Sills et al. 1997, 2001) and represent a possible formation channel for the young-seeming massive stars observed in the inner ~ 0.05 pc of the Milky Way's Galactic center (e.g., Ghez et al. 2003; Genzel et al. 2010b; Alexander 1999; Rose et al. 2023).

In addition to the relative speed between the stars, the outcome of a direct collision depends on the interplay of a number of initial conditions, including the impact parameter, mass ratio, and internal structures of the stars and therefore their ages. The effect of a collision on a star's mass and structure can only be fully understood using hydrodynamics simulations. Generally, simulations of collisional dynamics in nuclear star clusters have needed to make physically-motivated assumptions about collision outcomes (e.g., Mastrobuono-Battisti et al. 2021; Rose et al. 2022; Ashkenazy & Balberg 2024; Rose & Mockler 2025); over 10 Gyr of evolution, tens of thousands of collisions may occur within the cluster, making it computationally prohibitive to run a hydrodynamics simulation to predict the outcome each time. Some nuclear star cluster models (e.g., Rauch 1999; Rose et al. 2023) have leveraged fitting formulae developed from datasets of smoothed-particle hydrodynamics (SPH) simulations (as provided by, e.g., Lai et al. 1993). However, while outcomes like the mass loss from the stars and whether the collision results in a merger have been examined in detail, the effects of high-speed collisions on the trajectory of stars has been less wellstudied (for one of the few examples, see the appendix in Rauch 1999).

We present a new set of high-resolution SPH simulations of collisions between 1 M_{\odot} stars. We use our grid

of 236 simulations to build a physical intuition about the orbital effects of stellar collisions and develop fitting formulae to predict a star's post-collision velocity. We also re-visit fitting formulae for the mass loss and general collision outcome, e.g., if the collision destroys the stars, based on the literature. Furthermore, motivated by the vastness of the parameter space for direct collisions, which limits the effectiveness of even fitting formulae (see discussion in Freitag & Benz 2005), we use our two-dimensional grid as a testing ground for machine learning (ML) techniques to model stellar collisions. Similar techniques have been successfully applied to collisions in planet formation simulations (e.g., Winter et al. 2023; Crespi et al. 2024), and recently, Amaro Seoane (2025) modeled the SPH dataset for stellar collisions from Freitag & Benz (2005) using gradient-boosted regression trees. This paper is organized as follows:

In Section 2, we describe our SPH simulations and methodology. Section 3 provides a qualitative overview of the grid of collision outcomes. We then proceed to fitting formulae in Section 4. In Section 4.1, we describe the capture radius for a stellar merger to occur following a collision and find good agreement between our SPH dataset and the fitting formula from Lai et al. (1993). Section 4.2 focuses on the mass loss from the collisions. We develop fitting formulae for the effects of collisions on the stars' trajectories in Sections 4.3 and 4.4. In Section 5, we consider two different ML algorithms to model the SPH dataset: k-Nearest Neighbors and neural networks. We use classification in Section 5.1 to predict the category of collision outcome and regression in Section 5.2 to predict variables like the mass loss. Section 5.3 compares ML with our fitting formulae. We conclude in Section 6.

$\begin{array}{c} {\rm 2. \ \, SMOOTHED\text{-}PARTICLE \ \, HYDRODYNAMICS} \\ {\rm SIMULATIONS} \end{array}$

We use the SPH code StarSmasher (Gaburov et al. 2010; Rasio 1991) to simulate hyperbolic collisions between two 1 $\rm M_{\odot}$ stars. We obtain the structure of the star from a MESA profile at 5 Gyr from Kıroğlu et al. (2023). In our simulations, each star is represented with $N=10^5$ SPH particles that carry mass, position, velocity, and internal energy. The local resolution is set by an adaptive smoothing length assigned to each particle. We employ a Wendland C4 smoothing kernel (Wendland 1995) for hydrodynamic interpolation and for gravity softening. To handle shocks and suppress unphysical particle interpenetration, an artificial viscosity is used together with a Balsara-type switch (see Balsara 1995; Hwang et al. 2015). The particles are advanced using equations of motion obtained from a variational for-

mulation that enforces proper evolution of energy and entropy (Monaghan 2002; Springel & Hernquist 2002; Lombardi et al. 2006). Self-gravity in our calculations is evaluated by direct summation of particle-particle interactions on NVIDIA GPUs (Gaburov et al. 2010), consistent with energy-conserving formulations for particle-based gravity (Price & Monaghan 2007). Thermodynamics are modeled with an analytic equation of state that includes ideal gas and radiation pressure, as in Lombardi et al. (2006).

After each impact, we evaluate the material gravitationally bound to each star. Our determination of the final bound masses follows the iterative procedure in Lombardi et al. (2006). Guided by Nandez et al. (2014), the boundness criterion employs mechanical energy, rather than total energy: i.e., internal energy is excluded. As our collisions never produce a bound binary as the ultimate end state, a common-envelope component need not be considered. To determine the collision-induced velocity change and deflection angle, we propagate the relative two-body orbit from the final simulation snapshot to $r \to \infty$ and compute these quantities from the resulting asymptotic velocities of the two stars.

We explore a two dimensional parameter space of v_{∞} and r_p , where the former is the relative speed of the stars at infinity and the latter is the distance of closest approach between the stars. Generally, we sample velocities at intervals of 200 to 300 km/s from 100 to 5000 km/s. We sample r_p at intervals of 0.2 R_{\odot} from $r_p = 0$ (head-on collisions) to 1.8 R_{\odot} (grazing collisions), with some exceptions. Most notably, we include four simulations with $v_{\infty} = 10$, 100, 300 and 600 km/s for a close passage of 2.5 R_{\odot} to compare with expectations for tidal dissipation and tidal capture (e.g., Press & Teukolsky 1977; Lee & Ostriker 1986).

3. QUALITATIVE RESULTS

There are three possible qualitative outcomes for collisions between equal-mass stars:

- 1. Stellar merger: if the relative speed or impact parameter between the stars is sufficiently low, the stars can capture one another and merge. We refer to this as a "one star" outcome. Figure 1 shows snapshots from an example SPH simulation that resulted in a merger the first row.
- 2. Hit-and-run collision: a subset of the collisions have too high a speed or too large an impact parameter to result in a merger. These collisions are best described as "hit-and-run" types of encounters; the stars physically collide, but they are not able to capture each other. We refer to this out-

come as a "two star" case and show an example in the second row of Figure 1.

3. Complete destruction: if the relative speed is sufficiently high and the impact parameter small, the high kinetic energy of the impact can effectively destroy the stars, a "zero star" outcome. Approaching this limit of total destruction, collisions drive large mass loss from the stars. We show an example of a zero-star outcome in the last row of Figure 1.

All of the examples in Figure 1 have $r_p=0.2~{\rm R}_\odot$. However, by increasing v_∞ , we achieve different collision outcomes. We note that in cases of unequal stellar masses, a collision can destroy one star while the other survives (Lai et al. 1993; Gibson et al. 2025), beyond the scope of this study.

We show the results of our 236 SPH simulations in Figure 2. The upper left panel shows the general collision outcome for each simulation within our v_{∞} - r_p parameter space. The role of v_{∞} and r_p in determining the collision outcome can be gleaned from the figure. For example, the entire upper right part of the parameter space comprises hit-and-run collisions, while fully destructive collisions only occur for low r_p and high v_{∞} . We also plot a fitting formula (Eq. 1) for the boundary between mergers and hit-and-run collision win black, described in more detail in Section 4.1.

The mass loss from the stars also characterizes the collision outcome. The transition from one and two star cases to zero star cases occurs when the fractional mass loss from the system nears 100%. We show the mass loss from the system, expressed as a fraction $f_{\rm ML}$, for each of our simulations in the bottom left plot of Figure 2. In equal-mass hit-and-run collisions, both stars will experience the same mass loss due to symmetry arguments. As such, f_{ML} from the system is equal to the fractional mass loss from each star, $(M_{\star,i}-M_{\star,f})/M_{\star,i}$, where $M_{\star,i}=1~{\rm M}_{\odot}$. The mass loss is minimized for large r_{peri} and low v_{∞} .

In addition to the number of remnants and the mass loss from the system, we also examine the orbital effects of collisions. For mergers, the final star remains at rest in the center of mass frame; there is no asymmetric mass loss to impart a velocity kick. In simulations of dense stellar clusters, momentum conservation is used to treat collisions in this regime (e.g., Rodriguez et al. 2022; Rose & Mockler 2025). For zero star cases, the question of a star's final trajectory is rendered moot by its total destruction. We therefore focus our examination on the two star cases.

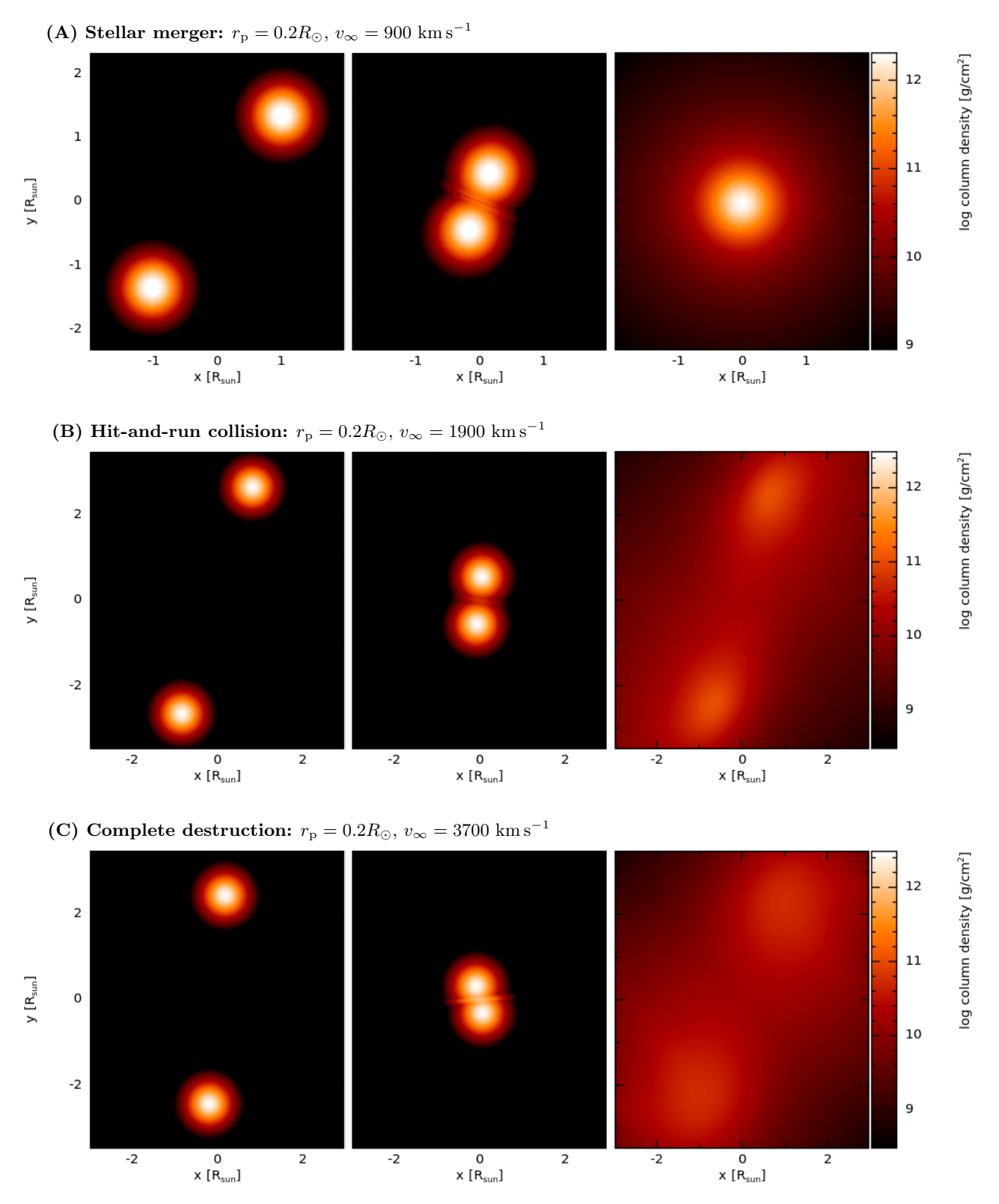


Figure 1. Various collisions of two identical $1 M_{\odot}$ stars. (A) The top row illustrates the case with $r_{\rm p} = 0.2 R_{\odot}$, $v_{\infty} = 900$ km s⁻¹, resulting in a stellar merger. (B) The second row of snapshots shows $r_{\rm p} = 0.2 R_{\odot}$, $v_{\infty} = 3700$ km s⁻¹, in which both stars remain, having been stripped by the collisions. (C) The third row is for $r_{\rm p} = 0.2 R_{\odot}$, $v_{\infty} = 3700$ km s⁻¹: although two separate overdense regions are seen in the final panel, both dissipate as time progresses, leaving no final stars. Color bars show column density on a logarithmic scale in g cm⁻².

We approach changes to the star's velocity vector in two parts: magnitude and direction. We quantify the former using the fractional decrease in speed, $\Delta v/v_{\infty}$, while deflection angle $\Delta\theta$ quantifies the change in direction. We show the fractional change in speed and deflection angle in the right column of Figure 2. The change in speed is maximized for small r_p and, to a lesser degree, small v_{∞} . In other words, collisions with the most physical overlap between the stars have the strongest effect on the speed, while for large v_{∞} , the stars have very little time to act on one another. Similarly, the deflection angle is largest for small v_{∞} because it is easier to deflect slower moving stars. Generally, the relationship between fractional mass loss and v_{∞} trends in the opposite direction as the velocity changes. Therefore, most collisions that lead to high $f_{\rm ML}$ tend not to affect the trajectory of the stars significantly.

4. FITTING FORMULAE

To complement our qualitative understanding of collisions as described above, we develop physically-motivated fitting formulae to quantify their effects on the stars.

4.1. Capture Boundary

For two stars to merge during a close interaction, they must dissipate their relative kinetic energy, $\propto v_{\infty}^2$, to become gravitationally bound. Stars have two possible mechanisms for dissipating kinetic energy during close interactions: tidal dissipation and shock dissipation. The first mechanism, tidal dissipation, is sufficient for the stars to capture each other only in the regime where $v_{\infty} \ll v_{esc}$ and can produce tight binary systems (e.g., Fabian et al. 1975; Press & Teukolsky 1977; Lee & Ostriker 1986; Ray et al. 1987; Kochanek 1992). As the relative speed between the stars increases, the system reaches a critical point where the stars must pass within a periapsis distance r_p less than the sum of their radii to become bound, necessitating a physical collision. As v_{∞} increases further, the distance of closest approach needed for the stars to become bound continues to decrease, and shocks become the dominant mechanism to dissipate the kinetic energy (e.g., Lai et al. 1993).

We define the capture radius as the critical distance of closest approach needed for the stars to become gravitationally bound. We find that the fit for the capture radius from Lai et al. (1993, see their equation 4) performs well in light of our new SPH data. We note that Lai et al. (1993) fit in terms of a dimensionless velocity parameter $v_{\infty}' = v_{\infty}/\sqrt{GM_{\star}/R_{\star}}$, while in this work, we typically fit in terms of the quantity v_{∞}/v_{esc} , where $v_{esc} = \sqrt{2GM_{\star}/R_{\star}}$ is the escape speed from the surface

of the star. Re-writing their equation to be consistent with our notation, we arrive at the general form:

$$\frac{r_{\text{cap}}}{R_1 + R_2} = A_{\text{cap}} \left(\frac{0.112}{v_{\infty}/v_{esc}} \right)^{\eta}, \tag{1}$$

where $A_{\rm cap}$ is a dimensionless constant, $\eta=0.18+\sqrt{v_{\infty}/(5.65v_{esc})}$, and R_1+R_2 is the sum of the radii of the two colliding stars. We remind the reader that in this work $R_1=R_2=R_{\odot}$. As v_{∞} becomes much less than v_{esc} , η approaches 0.18. Thus, Eq. 1 reproduces the tidal capture limit for n=3 polytropes at small v_{∞} (e.g., Press & Teukolsky 1977; Lee & Ostriker 1986; Lai et al. 1993).

Lai et al. (1993) fit $A_{\rm cap}$ for different values of a dimensionless parameter α , which they define to be $\propto M_{\star}$. While they only provide values of $A_{\rm cap}$ for $\alpha=1$ and 10, corresponding to M=5 and 50 ${\rm M}_{\odot}$, we extrapolate the value of $A_{\rm cap}$ for 1 ${\rm M}_{\odot}$ stars. Assuming a power-law fit to the values for equal-mass collisions in Lai et al. (1993) table 1, we find $A_{cap} \propto \alpha^{0.064}$, giving the relation $A_{cap}=0.95\times\left(\frac{M_{\star}}{5M_{\odot}}\right)^{0.064}$. Consequently, $A_{\rm cap}=0.857$ for 1 ${\rm M}_{\odot}$ stars. We plot the capture radius as a function of v_{∞} in the upper left panel of Figure 2 in black.

4.2. Fractional Mass Loss

The framework for understanding collision-driven mass loss from Lai et al. (1993) informs our initial approach to the fitting for this parameter. As described in their section 2.2, the mass ejected by a stellar collision should depend on the ratio of the kinetic energy, μv_{∞}^2 where μ is the reduced mass, to the binding energy of the stars. Furthermore, hyperbolic collisions eject shock-heated gas in quantities dependent on the stellar structure. For a head-on collision, the fractional mass loss from the system should roughly be $A + B \times v_{\infty}^2$.

As described in Section 3, we quantify the mass loss using the fraction $f_{\rm ML}=\frac{M_f-M_i}{M_i}$, where M_f (M_i) is the final (initial) mass of the system. For collisions of equal-mass 1 ${\rm M}_{\odot}$ stars, symmetry arguments demand that the total mass loss from the system is equivalent to the mass loss from each star, $f_{\rm ML}=\frac{M_{f,\star}-M_{\odot}}{M_{\odot}}$. We begin from a fit with the form $f_{\rm ML}=A+B\times v_{\infty}^a$. In a departure from previous studies in the literature (Lai et al. 1993; Rauch 1999), we fit the fractional mass loss for the one and two-star cases separately. While we focus on equal-mass collisions, future work may expand the fitting formulae to collisions with mass ratio $q\neq 1$. The mass loss from a merger product in the $q\neq 1$ regime can still be expressed as a single quantity. However, in hit-and-run collisions, stars of different masses will experience different degrees of mass loss, and the fit will

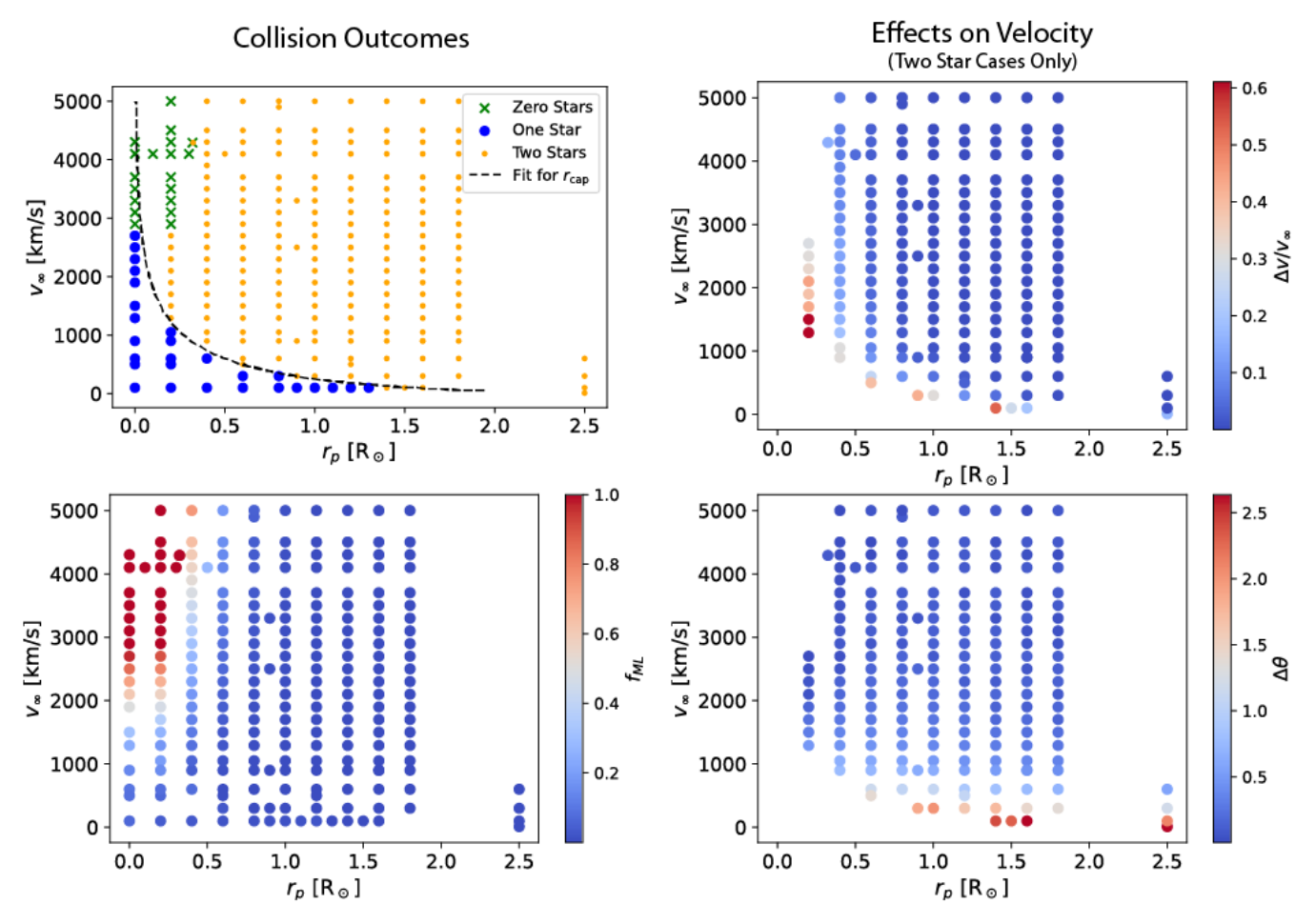


Figure 2. Parameters of interest from our grid of SPH simulations. Upper left: The general collision outcome for each pair of initial relative speed (v_{∞}) and distance of closest approach between the stars (r_p) sampled. Blue circles represent cases where the collision culminated in a merger, i.e., resulted a single star. Green crosses indicate where the collision destroyed both stars. Orange dots represent cases where the speed was too high or the impact parameter too large for the stars to capture one another and merge. We show the fit for the boundary between mergers and higher-speed "hit-and-run" type collisions in the black dashed line (Eq. (1), adapted from Lai et al. (1993)'s equation 4). Lower left: The fractional mass loss from the stars (f_{ML}) . A fractional mass loss of 1 indicates a complete disruption of the stars. Fractional mass loss is maximized for small impact parameter and high speed. Right column: The effects of high-speed collisions ("two star" cases) on the velocity vector of the stars. The upper panel shows the fractional decrease in speed $(\Delta v/v_{\infty})$ and the bottom panel, the deflection angle $(\Delta \theta)$. The deflection angle is maximized for low-speed collisions, while the fractional change in speed is maximized for smaller r_p , corresponding to more physical overlap between the stars.

need to be expanded to encompass the relationship between the mass loss fraction from the primary star and that of the secondary star.

For the merger regime in our simulation grid, we find that the fractional mass loss can be fit by:

$$f_{\rm ML} = \frac{0.0658}{1 + 3.85 \frac{r_p}{R_{\odot}}} + 0.0425 \left(\frac{v_{\infty}}{v_{\rm esc}}\right)^{2.08 + 2.19 \frac{r_p}{R_{\odot}}}.$$
 (2)

Here, we have normalized v_{∞} by the escape speed from the surface of the star, $\sqrt{2GM_{\odot}/R_{\odot}}$, a form which reflects the ratio of the kinetic energy of the collision to the binding energy of the stars. While we have normalized the periapsis distance by the radius of the star,

it is trivial to re-write the equation in a more generalized form that depends on $r_p/(R_1+R_2)$, or $2R_{\odot}$ for our system. The first term in Eq. 2 is the fit for parabolic collisions from Lombardi et al. (2002). Our fit therefore reproduces the expectation in the regime of $v_{\infty} \ll v_{esc}$. We note that since Eq. 2 can give values greater than 1, we take the maximum between 1 and Eq. 2 as the true mass loss.

The best fit for the two-star cases, or hit-and-run collisions, is:

$$f_{ML} = 0.12 e^{-4.17 \frac{r_p}{R_{\odot}}} \times \left(\frac{v_{\infty}}{v_{esc}}\right)^{2.23 - 1.39 \frac{r_p}{R_{\odot}}}.$$
 (3)

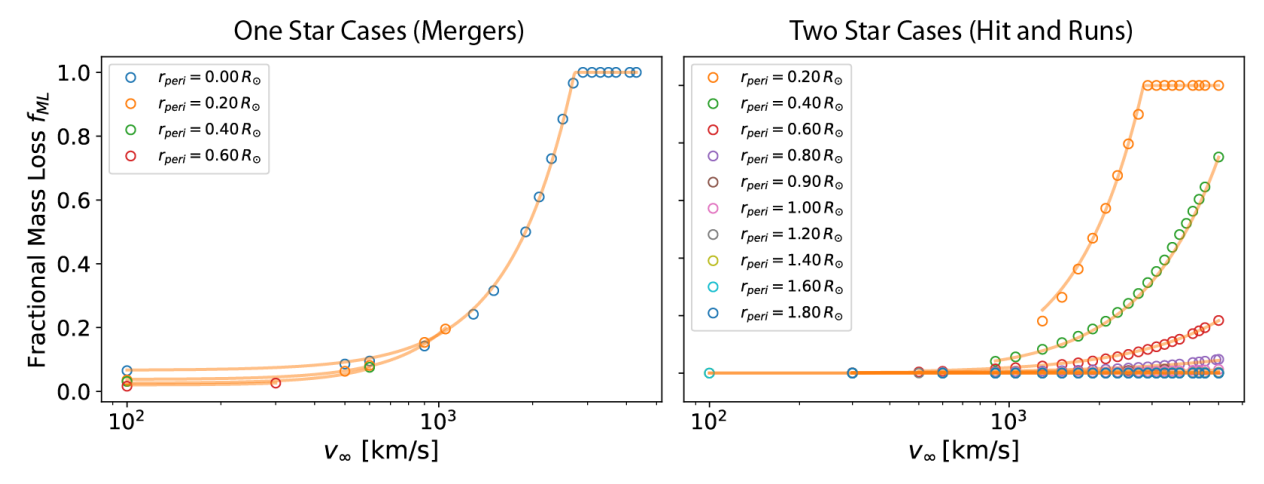


Figure 3. Fractional mass loss (f_{ML}) from the SPH simulations versus v_{∞} for different values of r_p . We divide the data up into mergers, or "one star", cases and hit-and-run type collisions, or "two star" cases. However, we also include relevant "zero star" cases – total destruction, $f_{ML} = 1$ – to show the transition between the other two classes and fully destructive collisions. The orange lines represent our fits from Eq. 2 (left) and Eq. 3 (right), which reproduce the transitions to $f_{ML} = 1$.

The fractional mass loss is maximized for close to headon collisions. To capture this behavior, we make the coefficient in the fit decay exponentially. As is the case for the merger fitting formula, the fractional mass loss is given by the maximum between Eq. 3 and 1.

We show our fitting formulae for mergers and hit-andrun collisions versus the SPH data in the left and right panels of Figure 3, respectively. The data points are colored by r_p , while the orange curves show the fitting formulae predictions for the fractional mass loss. Both Eq. 2 and Eq. 3 are accurate to within $\sim 4\%$ percent for all of our data. Furthermore, we reproduce the transition from surviving stars to total destruction ($f_{\rm ML}=1$) for the head-on case ($r_p=0$) in the left panel. Collisions with $r_p>0$ must first transition from mergers to two-star collisions, shown on the right, before reaching the threshold for full destruction. It is therefore Eq. 3, the fitting formula for two-star collisions, that reproduces the transition to fully destructive collisions in the regime where $r_p>0$.

4.3. Deflection Angle

Hyperbolic encounters between point particles provide an analytical framework within which we can understand two-star collisions. In a purely hyperbolic encounter without a physical collision, stars will be deflected by angle $\theta_{\rm hyp}$ in their center of mass frame, though the speed of the stars at infinity will be unchanged due to energy conservation. The deflection angle can be written as:

$$\theta_{\text{hyp}} = 2\arctan(b_{90}/b) , \qquad (4)$$

where b is the impact parameter and b_{90} is the impact parameter needed for a 90° deflection. b_{90} equals

 $G(2M_{\odot})/v_{\infty}^2$, where we have taken the mass of each star to be 1 M_{\odot} (e.g., Binney & Tremaine 2008, equation 3.52). As r_p increases, we approach the limit where the two stars barely graze, and the deflection angle $\Delta\theta$ should approach $\theta_{\rm hyp}$.

The limiting case described above motivates our fitting formula. Specifically, we find that a function with the form:

$$\Delta \theta = \left(1 + Ae^{-\left(\frac{r_p}{R_{\odot}}\right)^2} - B\frac{v_{\infty}}{v_{\rm esc}}e^{-a\left(\frac{r_p}{R_{\odot}}\right)^2}\right)\theta_{\rm hyp}, (5)$$

fits the data well with $A=0.16,\,B=0.35,\,a=2.5,$ and $\theta_{\rm hyp}$ given by Eq. 4. While Eq. 4 is written to depend on the impact parameter at infinity, b, it is related to r_p by:

$$b^2 = r_p^2 + 2G(M_1 + M_2)r_p/v_\infty^2 , (6)$$

where once again we have $M_1 = M_2 = 1 \text{ M}_{\odot}$. We show the predictions of this fitting formula compared to the SPH data and θ_{hyp} in Figure 4 for nine values of r_p . The root-mean-squared error of the fitting formula predictions is 0.022 radians. The fitting formula is accurate to within 4 degrees for all of our SPH data and within 1 degree for 94% of the data. Crucially, this equation reproduces $\theta_{\rm hyp}$ in the limit $r_p \gtrsim 2~{\rm R}_{\odot}$ because the exponential terms become small. We also find that the hyperbolic deflection angle for point particles (Eq. 4) is accurate to within 0.1 radians, or 6 degrees, for $r_p > 0.6 \text{ R}_{\odot}$. This result suggests that despite experiencing a physical collision, stars in this regime behave far more like point particles than previously assumed in the literature (e.g., Yu & Tremaine 2003; Rose & Mockler 2025). We attribute this behavior to the fact that

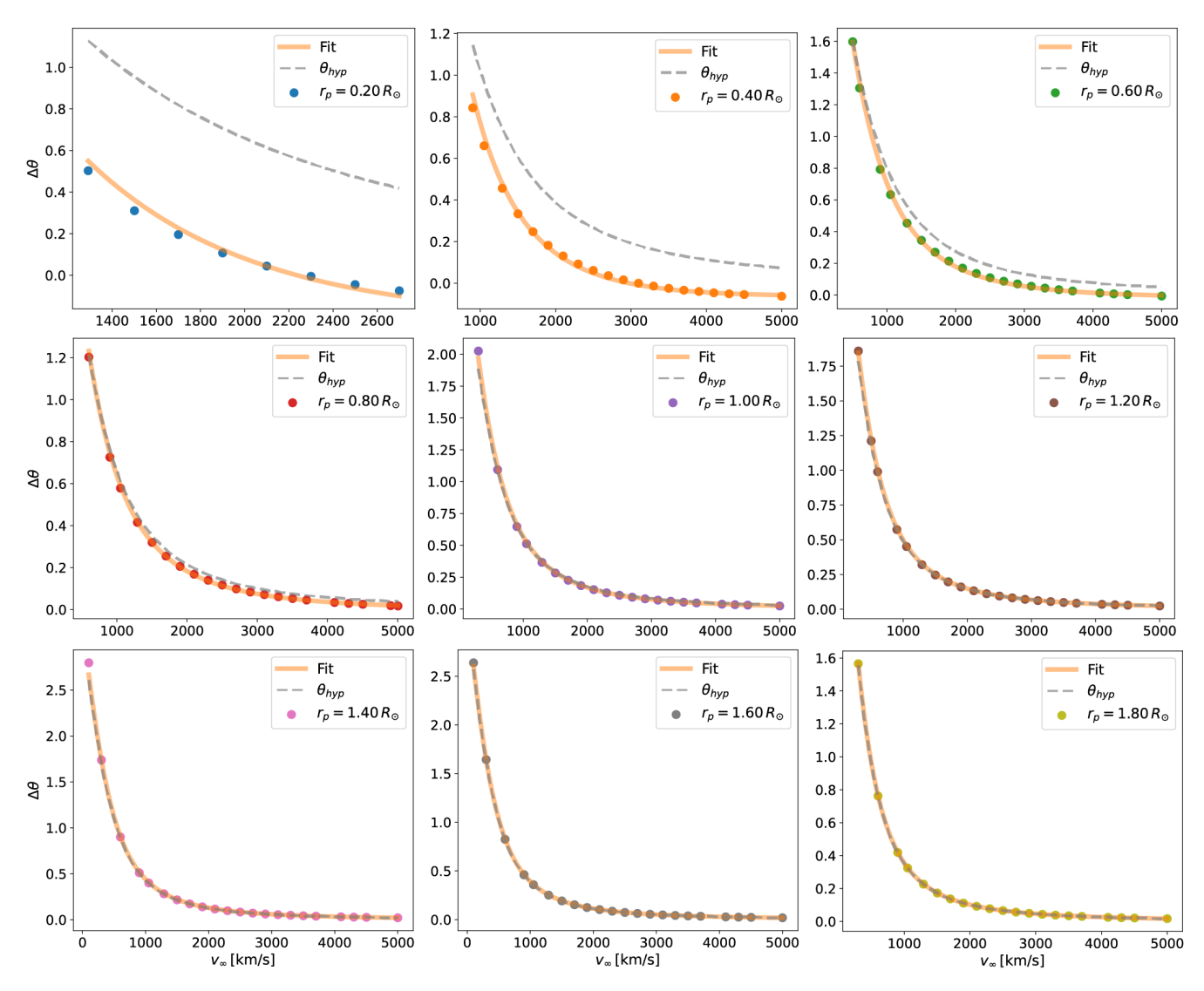


Figure 4. Deflection angle following a hit-and-run (two-star) collision versus v_{∞} for all of our values of periapsis with more than 5 data points, which are the SPH data used to tailor the fitting formula given by Eq. 5. Dots represent the SPH results, while the grey dashed curve is the deflection angle for a hyperbolic encounter between point particles (Eq. 4). The orange solid curves represent the predictions of our fitting formula (Eq. 5), which is generally accurate to within 4 degrees for all of our data. We note that for $r_p > 0.6~\mathrm{R}_{\odot}$, the equation for a purely hyperbolic encounter predicts the deflection angle to within 0.1 radians, or 6 degrees.

most of the star's mass is concentrated near its core, and for larger periapses ($r_p > 0.6~{\rm R}_{\odot}$), only the more diffuse envelopes of the stars interact.

We note that for $r_p=0.2~{\rm R}_\odot$ and $0.4~{\rm R}_\odot$, the deflection angle becomes negative for very high v_∞ (see first and second panels in Figure 4). Here, we define a positive deflection angle to denote a deflection towards the other star, as would occur in a purely gravitational interaction. A negative deflection angle can occur for the high-speed encounters that push right up to, but do not cross, the threshold of complete disruption while still yielding a two-star outcome. Collisions in this regime

generate significant shocks and ejecta, and the bound mass that remains within each star recoils from the impact. A negative deflection angle is tantamount to the stars "bouncing" off of each other. We also note that at the other extreme, low speed and larger r_p collisions, Eq. 4 – for point particles – slightly under-predicts the deflection angle. For an example, see the last SPH data point versus the grey dashed line for $r_p=1~{\rm R}_{\odot}$ or $r_p=1.4~{\rm R}_{\odot}$ subplots in Figure 4. Dissipation during these $v_{\infty}=100~{\rm km/s}$ collisions means the stars slow down by $\gtrsim 30\%$ (see Section 4.4 below). It is easier to deflect slower moving stars. However, Eq. 4 only de-

pends on v_{∞} . The reduction of the stars' speed during the collision translates to a slight boost in the deflection angle relative to the prediction from Eq. 4.

4.4. Fractional Change in Speed

In hit-and-run collisions, a star can both change direction (Section 4.3) and speed. As touched on in Section 4.2, there are two ways of dissipating kinetic energy from the system: tidal dissipation and shock dissipation. The change in kinetic energy due to tidal dissipation can be described as:

$$\Delta E_{\text{tidal}} = \left(\frac{GM_1}{R_1}\right)^2 \left(\frac{M_2}{M_1}\right)^2 \sum_{l=2,3} \left(\frac{R_1}{r_p}\right)^{2l+2} T_l(\eta)(7)$$

where l is the spherical harmonic and $T_l(\eta)$ are dimensionless functions of $\eta = \left(\frac{M_1}{M_1 + M_2}\right)^{0.5} \left(\frac{r_p}{R_1}\right)^{1.5}$ that quantify the deposition of the kinetic energy into the star's internal oscillations (e.g., Press & Teukolsky 1977; Lee & Ostriker 1986). For our collisions, we can adapt the above equation to:

$$\Delta E_{\text{tidal}} = \frac{GM_{\odot}^2 R_{\odot}^5}{r_n^6} T_2(\eta) + \frac{GM_{\odot}^2 R_{\odot}^7}{r_n^8} T_3(\eta).$$
 (8)

While in principle this calculation involves summing over all spherical harmonics, the other terms prove to be insignificant compared to quadrupole and octupole tides (e.g., Lee & Ostriker 1986). From ΔE , the change in the star's speed can be found using:

$$\Delta v_{\text{tidal}} = \sqrt{E_i/\mu} - \sqrt{(E_i - \Delta E_{\text{tidal}})/\mu},$$
 (9)

where $E_i = \frac{1}{2}\mu v_{\infty}^2$ and μ is the reduced mass. In the limit of low-speed grazing collisions, we should recover a change in speed given by Eq. 9.

Mardling & Aarseth (2001) extend this framework for tidal dissipation to hyperbolic encounters by substituting ζ for η . They define $\zeta = \eta \sqrt{2/(1+e)}$, where e is the eccentricity of the orbit between the two stars. This equation recovers η for parabolic encounters, while also accounting decreased tidal dissipation at large v_{∞} . We opt to use ζ in place of η when predicting the change in speed for our hyperbolic collisions using the fitting formula below. However, we note that both η and ζ are less than 2 for a physical collision.

We treat the change in speed of the stars by breaking it into two components, a tidal contribution and a collision contribution:

$$\frac{\Delta v}{v_{\infty}} = \left(\frac{\Delta v}{v_{\infty}}\right)_{\text{tidal}} + \left(\frac{\Delta v}{v_{\infty}}\right)_{\text{coll}}.$$
 (10)

For grazing encounters, $\left(\frac{\Delta v}{v_{\infty}}\right)_{\text{tidal}}$ should dominate and the collision term should approach zero. Furthermore,

for close passages that are not physical collisions, our fitting formula should recover the expectation from Press & Teukolsky (1977) and Lee & Ostriker (1986).

We begin by fitting $\Delta v/v_{\infty}$ from our SPH dataset for cases with $r_p>1R_{\odot}$ with a tidal term given by combining Eq. 8 and 9. In this regime, the mass loss is negligible (see Figure 3) and μ can be taken as constant. Specifically, we fit the values of T_2 and T_3 to reproduce our data. To ground our fit in the limiting case of a close encounter, we calculate the actual values of T_2 and T_3 based on our star's MESA model using GYRE for the relevant eigenfrequencies and eigenfunctions (for GYRE, see Townsend & Teitler 2013; Townsend et al. 2018; Goldstein & Townsend 2020; Sun et al. 2023). The above calculation yields similar values to T_2 and T_3 for an n=3 polytrope as shown in Lee & Ostriker (1986). We ensure that as r_p becomes > 2 R_{\odot} , our fits for T_2 and T_3 converge on the GYRE data.

We fit both T_2 and T_3 with sixth order polynomials in terms of a dimensionless number η (or ζ). In order of highest to lowest order term, $T_{2,\mathrm{fit}}(\eta)$ has the coefficients:

$$[0.3082, -3.091, 4.719, -4.510, -0.7109, -1.584]$$

while $T_{3,\text{fit}}(\eta)$ has the coefficients:

$$[4.246, 9.556, 7.428, -4.699, -17.09, 5.967, -2.067].$$

We plot $T_{2,\mathrm{fit}}(\eta)$ and $T_{3,\mathrm{fit}}(\eta)$ as well as the GYRE values on the left in Figure 5. We confirm that for $T_{2,\mathrm{fit}}$ and $T_{3,\mathrm{fit}}$, the tidal term in Eq. 10 becomes negligible for $r_p < 1 \,\mathrm{R}_{\odot}$.

We took cues for the shape of $(\Delta v/v_{\infty})_{\text{coll}}$ from the SPH data for $r_p = 0.2 \text{ R}_{\odot}$, where the collision term should dominate. We find that the collision contribution to Eq. 10 can be fit using a sum of power-laws:

$$\left(\frac{\Delta v}{v_{\infty}}\right)_{\text{coll}} = (10^A) \left(\frac{v}{v_{\infty}}\right)^{-a} + (10^B) \left(\frac{v}{v_{\infty}}\right)^{-b}.(11)$$

A can be computed using a sixth order polynomial in terms of $\frac{r_p}{R_{\odot}}$ with coefficients:

$$[-53.03, 130.5, -64.13, -91.30, 121.8, -53.93, 8.145],\\$$

while $\log_{10} a$ can also be represented by a sixth order polynomial in terms of $\frac{r_p}{R_{\odot}}$ with coefficients:

$$[-18.60, 46.79, -22.74, -33.37, 42.43, -17.09, 2.865]$$

The second power-law in Eq. 11 has b = 0.632 and $B = 0.874 - 2.596 \frac{r_p}{R_{\odot}}$.

We show our full fitting formula, Eq. 10, versus the SPH data on the right in Figure 5. The maximum error for the fit is $\lesssim 10\%$. In fact, there is a single data

point at $r_p=1.4~{\rm R}_{\odot}$ and $v_{\infty}=100~{\rm km/s}$ which is under-predicted by more than a few percent by the fitting formula. Otherwise, the fitting formula predicts the change in speed within 2% for the SPH data.

5. MACHINE LEARNING

ML techniques offer tantalizing new prospects for modeling large datasets. In this section, we explore the efficacy of ML models compared to physically-motivated analytic expressions like fitting formulae. In our simple two-dimensional parameter space, we test both the commonly used k-Nearest Neighbors (kNN) algorithm and a neural network (NN). We use the SciKitLearn package for the former and PyTorch for the latter. We train classifiers to predict the collision outcome, where labels 0, 1 and 2 denote the number of remnants. Regression is required to predict continuous variables like the fractional mass loss or deflection angle.

For both ML techniques, the input data includes $\log_{10} v_{\infty}$ and r_p . Furthermore, we scale the data so that the values lie between 0 and 1 for kNN, and we standard normalize the data for the NN. For the NN, we split the dataset into 60% training data, 20% validation data, and 20% testing data. Validating the model during the training loop helps prevent over-fitting of the training data, while the testing data is used to measure the performance of the ML model on unseen data. When splitting our data into the different subsets, we ensure that each class label is represented proportionate to its overall prevalence in the dataset. In other words, if mergers represent the outcome in roughly 5% of all of our SPH simulations, they will also represent roughly 5% of the training, testing, and validation datasets. We similarly split the data into 80% training data and 20% testing data for the kNN model. However, for kNN, we combine training and validation into one dataset and perform cross-validation within a grid search, described in more detail below.

5.1. Classification

The kNN algorithm is an intuitive and effective approach to modeling data (Cover & Hart 1967). It predicts the class of a particular data point based on the class of a specified number k of its closest neighbors. To optimize the algorithm for our dataset, we perform a grid search with five-fold cross validation to find the best hyperparameters for the model. We save the model with the highest balanced accuracy score on the validation set. In the grid search, we consider five options for the number of neighbors (3,5,7,9, and 13); uniform and inverse-distance weights for those neighbors; Minkowski and Chebyshev metrics; and values of

p=1 and p=2 for the power parameter. We note that the power parameter values are only applicable to the Minkowski metric, with p=1 corresponding to the Manhattan distance and p=2 corresponding to the Euclidean distance. The Chebyshev metric takes the maximum difference between any of the coordinates, in this case, either along the r_p or $log_{10}(v_\infty)$ axes. The grid search returned the Minkowski metric with p=1, 3 neighbors and uniform weights.

NNs perform a series of transformations and activation functions to map input variables onto target output variables. Our NN has two hidden layers with 64 and 8 neurons, each followed by a Rectified Linear Unit (ReLU) activation layer (e.g., Fukushima 1969; Glorot et al. 2011; Maas et al. 2013; Agarap 2018). We set the learning rate to 0.1 and train the NN over 5000 epochs. We use Stochastic Gradient Descent as our optimization algorithm (e.g., Robbins & Monro 1951; Rumelhart et al. 1986) with a cross entropy loss function and verify throughout the training loop that both the training and validation losses decrease.

We juxtapose our best performing kNN model and NN in Figure 6. The first row shows our SPH data plotted over the decision boundaries of our models. For kNN, the misclassified testing data fall near the model's decision boundary, separating the one and two star collision outcomes. We show the confusion matrices in the second row of Figure 6. As can be seen from the figure, the NN out-performs our kNN model. The accuracy of our best kNN model on the testing data was 95.8%. However, the balanced accuracy is a better measure of the model's performance when one outcome is over-represented in the dataset, as is the case for hit-and-run collisions in our grid. This metric is calculated by averaging the prediction accuracies of the model for each class. The kNN model has a balanced accuracy score of 86.7% on the testing data. Our NN model, in contrast, has a balanced accuracy of 100% on the testing data.

5.2. Regression

Similar to our approach to classification, we find the best kNN model for regression using a grid search. The hyperparameters considered are the same as in Section 5.1. We repeat the grid search for each target variable, $f_{\rm ML}$, $\Delta\theta$, and $\Delta v/v_{\infty}$, in case they each benefit from different hyperparameters and use the kNN model with the lowest mean squared error (MSE). The hyperparameters returned for each target variable are listed

We also tried learning rates of 0.01 and 0.001 and found that they yielded similar performance so long as we increased the number of epochs; the loss rate simply took longer to plateau.

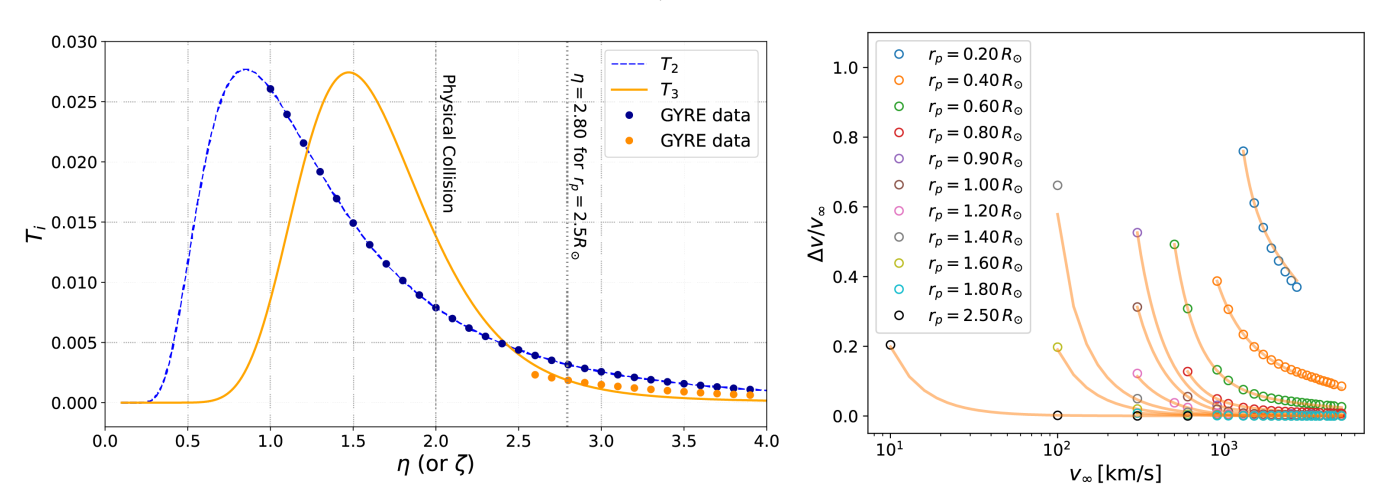


Figure 5. On the left, we show our $T_{2,\mathrm{fit}}$ and $T_{3,\mathrm{fit}}$ for Eq. 8, which are dimensionless functions that quantify a star's internal response to a tidal field. For $r_p > 2R_{\odot}$, our fits begin to converge with T_2 and T_3 as calculated for tidal capture using GYRE. On the right, we compare our fitting formula for the change in speed with the SPH data for hit-and-run collisions. The orange curves show our fitting formula, while the open circles represent the SPH data.

Table 1. Hyperparameters for the best-performing kNN model for each target variable.

Mode	Target Variable	\mathbf{k}	\mathbf{Metric}	${\bf Weights}$	\mathbf{p}
Classification	Number of remnants	3	Minkowski	Uniform	1
Regression	Fractional mass loss $(f_{\rm ML})$	5	Chebyshev	Inverse distance	NA
Regression	Deflection angle $(\Delta \theta)$	3	Minkowski	Inverse distance	2
Regression	Fractional speed change $(\Delta v/v_{\infty})$	3	Chebyshev	Inverse distance	NA

k indicates the number of neighbors.

The hyperparameter p is not applicable (NA) for the Chebyshev metric.

Table 2. Performance of different methods for predicting collision outcomes and properties.

Method	RMSE $(f_{\rm ML})$	${f MAE}~(f_{ m ML})$	RMSE $(\Delta \theta)$	$\mathbf{MAE}\ (\Delta\theta)$	RMSE $\left(\frac{\Delta v}{v_{\infty}}\right)$	$\mathbf{MAE}\left(rac{\Delta v}{v_{\infty}} ight)$
k-Nearest Neighbors	0.013	0.07	0.066 rad	$0.21 \mathrm{\ rad}$	0.034	0.21
Neural Network	0.008	0.03	0.006 rad	$0.02 \mathrm{\ rad}$	0.014	0.08
Fitting Formulae	0.007	0.04	0.02 rad	0.06 rad	0.007	0.08

We indicate the RMSE and maximum absolute error (MAE) for each method and target variables. While these metrics are unit-less for the fractional mass loss and change of speed, they have units radians for the deflection angle.

in Table 1. We note that all regression models showed preference for inverse-distance weighting.

We also use a NN to predict the mass loss and velocity effects of the collision. Our NN has three layers with 128, 64 and 32 neurons each, and uses ReLU as activation functions. We use the MSE as the loss function. We train the NN over 2000 epochs with a learning rate of 0.01 and an Adaptive Moment Estimation (Adam) optimization algorithm (Kingma & Ba 2014; Loshchilov & Hutter 2017).

We evaluate and compare these two methods using the root MSE (RMSE) of their predictions for the testing data. The RMSE for $f_{\rm ML}$, $\Delta\theta$, and $\Delta v/v_{\infty}$ for kNN were 0.041 (unit-less), 0.066 radians, and 0.034 (unit-

less), respectively. The NN delivered lower RMSE values across the board, at 0.008, 0.006 radians, and 0.014 for the target variables in the order listed above. We list these values in Table 2 for easy comparison. However, in physical systems, we also must care about the absolute errors and how they vary over the parameter space: the RMSE for a predictive model may be low, but it can still be inaccurate in regimes where the deflection angle or fractional mass loss are significant.

Figure 7 displays the absolute errors of the kNN models and the NN for the testing data over the parameter space. As is our convention, circles represent the training and validation data, while triangles represent the testing data. We color-code the testing data accord-

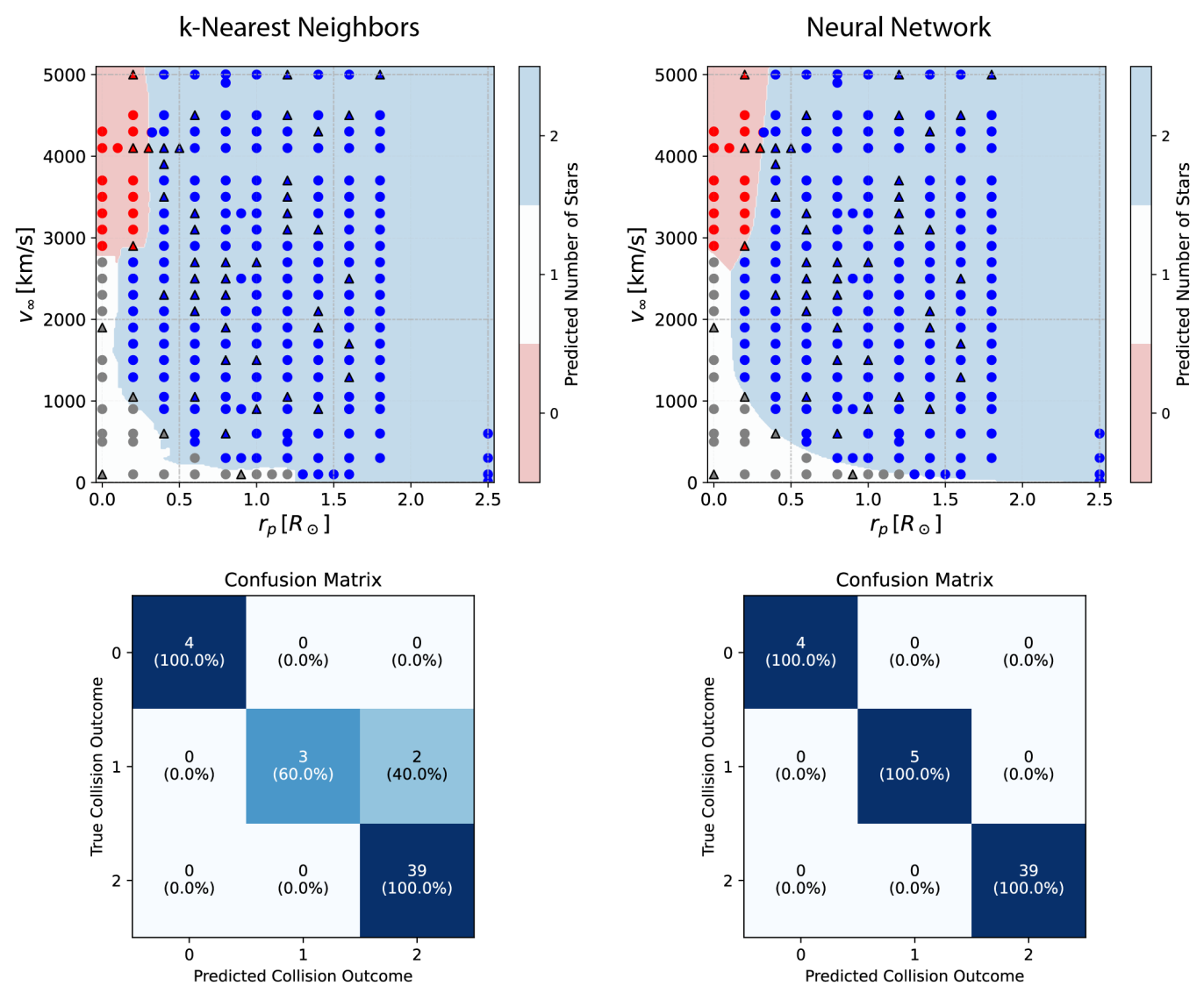


Figure 6. We juxtapose the results of the kNN algorithm, on the left, with our NN, on the right, for classification. In the first row, we show the grid of SPH data plotted over the decision boundaries predicted by the ML models. Circles represent the datasets used for training the ML models, while triangles represent the testing dataset. Grey denotes a merger, blue a two-star outcome (hit-and-run collision), and red a zero-star outcome (total destruction). The color scheme is similar for the decision boundaries, though we use white for one-star outcomes for readability. In the bottom plots, we show the confusion matrix for each ML technique, which shows the ML model's performance across each class of outcome. The percentages in each square indicate the fraction of the data that were correctly or incorrectly classified for each true number of remnants. Because the NN model has 100% accuracy, the off-diagonal terms in its confusion matrix are zero. The NN out-performed kNN. The misclassified data from the latter model always lie near the decision boundaries.

ing to the absolute error of the prediction compared to the true value. Consistent with our findings for classification and the regression MSEs, the NN has smaller absolute errors compared to kNN. We list the maximum absolute error for each target variable in Table 2. For example, kNN predicts the deflection angle to within 0.2 radians, while the NN is accurate to within 0.02 radians. However, both models have the largest absolute errors near boundaries between the collision outcome classes.

The regions in the bottom left quadrants of the plots, near the boundary between mergers and hit-and-run collisions, are also where variables like the deflection angle and fractional change in speed exhibit the greatest variation and range in values. Both models tend to be very accurate in the upper right quadrant of the parameter space, where the fractional mass loss, deflection angle, or fractional change in speed are all roughly zero (see Figure 2).

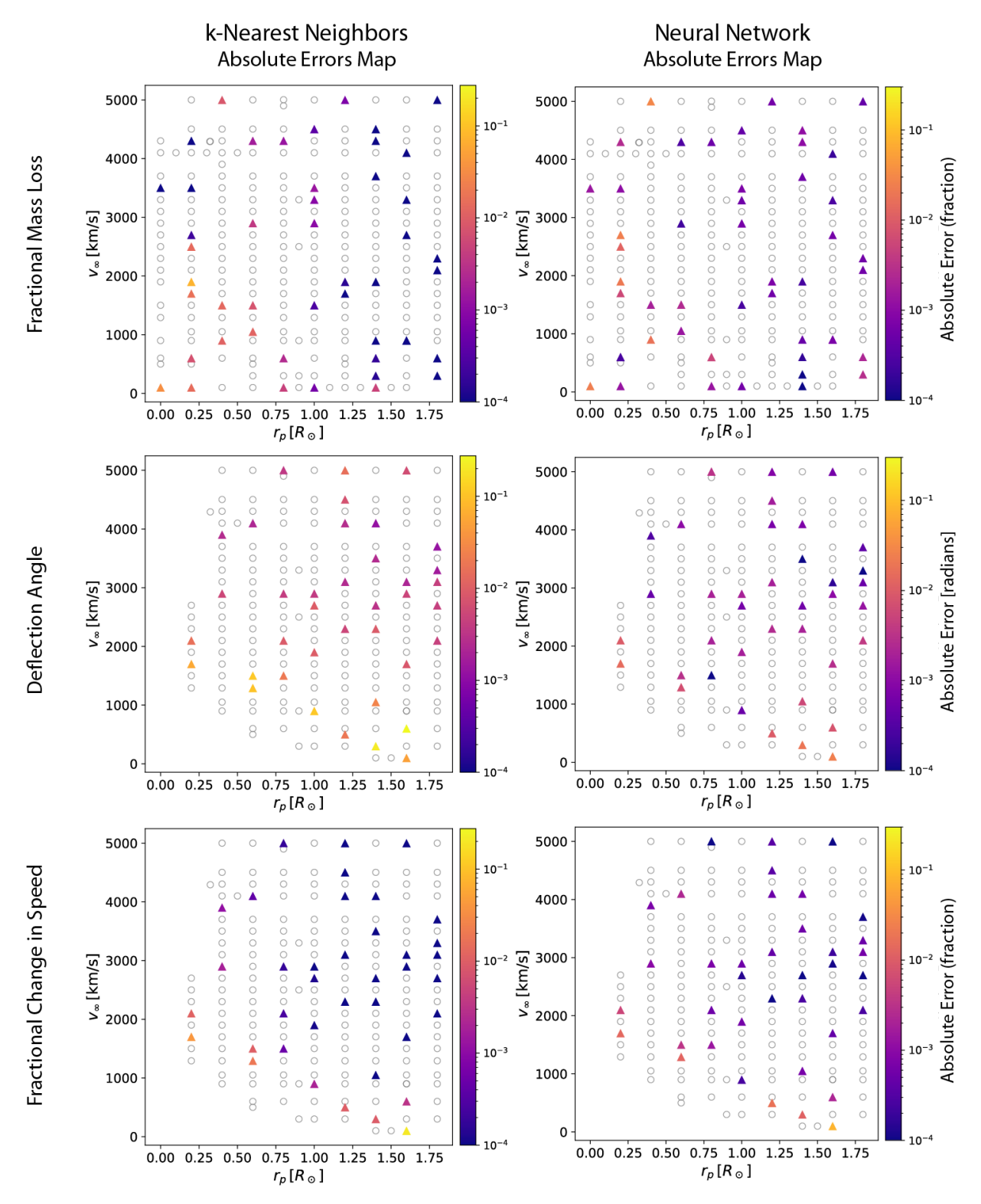


Figure 7. We show a grid of the ML regression errors in our v_{∞} versus r_p parameter space, similar in layout to those in Figure 2. Per our convention in other figures, circles represent training data, and triangles represent testing data. The triangles are color-coded by the absolute error of the prediction compared to the true value. Each row corresponds to one of our target variables. We stress that the absolute error for the fractional mass loss and fractional change in speed is unit-less and can be understood as a fractional error, or a percent error if multiplied by 100. However, the absolute error in deflection angle has units radians. The kNN model produced larger absolute errors compared to the NN. For both methods, the absolute errors were larger near the boundaries between classes, for example where the outcome transitions from mergers to a two star outcome.

5.3. Comparing Machine Learning and Fitting Formulae

ML and fitting formulae both have merits when it comes to modeling large sets of data. As analytic expressions, fitting formulae make it easy to check limiting cases and facilitate a physical understanding of the system. However, while we have chosen to focus on sampling a two-dimensional parameter space $(r_p \text{ and } v_\infty)$ in detail, the outcome of a collision also depends on the mass ratio and type of the colliding objects, their structures, and ages. In dense stellar environments, the types of collisions are as diverse as the stellar and compact object populations that reside there. Depending on the behavior of the variable being fitted and the vastness of the parameter space, fitting formulae can become increasingly cumbersome to formulate and to implement. ML therefore represents a promising alternative for modeling collisions in dense stellar environments, and forthcoming work by González Prieto et al. (in prep) is performing a detailed comparative analysis of various ML algorithms across a broader parameter space.

In this section, we assess whether ML can out-perform analytic equations which have been expressly tailored to our SPH dataset. As the NN proved more accurate than our kNN model, we use it for this comparison. The RMSE for our fitting formulae predictions compared to the SPH data were 0.007 and 0.009 for the fractional mass loss from the mergers and hit-and-run collisions (Eq. 2 and 3, respectively); 0.02 radians for the deflection angle (Eq. 5); and 0.007 for the fractional speed change (Eq. 10). These values are included in Table 2 for comparison to the ML methods, though in the table, we calculate a RMSE for both $f_{\rm ML}$ fitting formulae predictions combined.

Furthermore, we use Figure 8 to visualize their relative performances for the fractional mass loss (first row), deflection angle (second row), and fractional change in speed (third row). The pink dots represent the predicted value of each target variable from the fitting formulae versus their true value. The blue triangles represent the same for the testing dataset from the NN. To guide the eye, we include a dashed red line indicating where the prediction equals the true value. The absolute error of the prediction is given by the vertical distance between the point and the dashed line. While not shown to avoid over-crowding Figure 8, the NN predictions for the training and validation data exhibit a similar high degree of accuracy.

We find the performance of the NN to be on par and in some cases exceeding the fitting formulae. For all target variables, the maximum absolute error from the NN was less than or equal to the maximum absolute error from the fitting formulae. For the fractional change in speed, both the fitting formula and the NN have a large absolute error (under 10%) for a single data point. What these two data points have in common is that they both lie very near the capture boundary between one and two star outcomes: at $r_p=1.6~{\rm R}_{\odot}$ and $v_{\infty}=100~{\rm km/s}$ for the NN and $r_p=1.4~{\rm R}_{\odot}$ and $v_{\infty}=100~{\rm km/s}$ for the fitting formula. The accuracy of the fitting formulae and NN for the fractional mass loss are nearly identical, and the NN predicts the deflection angle with greater accuracy at low v_{∞} (see discussion at the end of Section 4.3) compared to both Eq. 5, the fitting formulae, and Eq. 4, the deflection angle for point particles experiencing a hyperbolic encounter.

6. CONCLUSION

Stellar collisions are ubiquitous in nuclear star clusters, where they can lead to the formation of unusual stellar populations and drive the production of transient events. We explore a two-dimensional parameter space in r_p and v_∞ for equal mass collisions between 1 $\rm M_\odot$ stars using the SPH code StarSmasher. We sample initial relative speeds between the colliding stars ranging from 100 to 5000 km/s, encapsulating the velocities expected within the sphere of influence of a SMBH. We sample the distance of closest approach, or periapsis r_p , of the encounter between 0 and 1.8 $\rm R_\odot$ for a physical collision. We supplement our dataset of physical collisions with four simulations of close passages, $r_p=2.5~\rm R_\odot$, to understand how the kinematics of collisions relate to expectations from tidal dissipation.

We begin by categorizing the collisions by qualitative outcome, which can be classified according to the number of collision remnants. In the first case, the stars are able to capture each other and merge, producing a single star. In the second case, the relative speed between the stars is either too high or the periapsis too large for the stars to capture one another and merge. We refer to these cases as hit-and-run type collisions, and they result in two collision remnants. Lastly, the collision can completely destroy the stars, leaving behind zero collision remnants. These collisions typically have large v_{∞} and small r_p .

We use our two-dimensional grid to build a physical intuition about the effects of stellar collisions and develop fitting formulae for three key properties of the collision remnants. The first property is $f_{\rm ML}$, the fractional mass loss, which quantifies the mass ejected from the system during the collision. The second two quantities relate to the kinematics of the collision remnants. In collisions with symmetric mass loss, as is the case for our equalmass collisions, the merger product remains at rest in

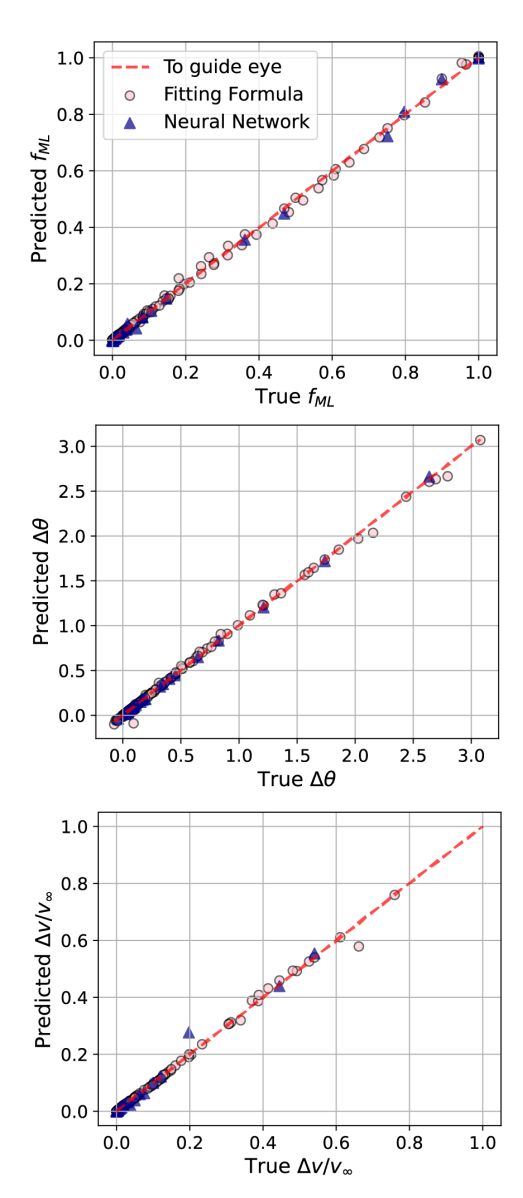


Figure 8. We juxtapose the predictions of our NN with those of the fitting formula. The NN predictions for the testing data versus the true values are shown in dark blue triangles. The pink circles represent the fitting formula predictions versus their true values. We also include the dashed red line to guide the eye. The closer to this line the points fall, the more accurate the prediction. The absolute error of the prediction is given by the vertical distance between the point and the line. For all of our target variables, the NN and fitting formulae have comparable accuracy.

the center of mass frame. In hit-and-run collisions; however, the stars continue along some modified trajectory. We understand changes to the stars' velocity vectors in two parts: the change in speed and the deflection angle. Lastly, we use our grid to test two ML algorithms, kNN and a NN, and we compare the accuracy of our best ML model to the fitting formulae. We summarize our results below:

- 1. Capture Boundary: The capture boundary separates mergers from hit-and-run collisions. For a given value of v_{∞} , there is some critical r_p within which the stars must pass to dissipate their relative kinetic energy and become a bound system. We find that the fitting formulae from Lai et al. (1993) accurately predicts the capture radius for our simulation grid after a simple scaling of their $A_{\rm cap}$ fitted constant to make it applicable to $1~{\rm M}_{\odot}$ stars. The formula can be found in Eq. 1. We note that the boundary transition to fully destructive collisions is given by the fitting formulae for the fractional mass loss, below, when it becomes equal to 1.
- 2. Fractional Mass Loss: The fractional mass loss from the system is defined as $\frac{\Delta M}{M_1+M_2}$. As described above, our collisions have $M_1=M_2=1~{\rm M}_{\odot}$. Due to symmetry arguments, fractional mass loss from the system is equivalent to the fractional mass loss from each of the stars. We fit the $f_{\rm ML}$ for one and two star collision outcomes separately, though we begin with an equation of the form $f_{\rm ML}=A+B\left(\frac{v_{\infty}}{v_{\rm esc}}\right)^a$ for both. For nearly head-on collisions, a is approximately 2. The full fitting formulae are given by Eq. 2 and 3. The fit for mergers, Eq. 2, reproduces the expected mass loss for parabolic collisions $(v_{\infty} \ll v_{\rm esc})$ from Lombardi et al. (2002). The fitting formulae are accurate to with 4% for all of our SPH data points.
- 3. **Deflection Angle:** Hyperbolic encounters between point particles informs our fitting formula for the deflection angle of the stars following a hit-and-run collision. Our fitting formula is given by Eq. 5, accurate to within 4 degrees for all of our SPH data. Furthermore, we find that the deflection angle is well-approximated by the point particle limit (Eq. 4) for $r_p > 0.6 \text{ R}_{\odot}$ because most of a star's mass is concentrated at its center. Generalizing this behavior to all main-sequence stellar collisions, we expect the hyperbolic encounter limit, Eq. 4, to be accurate to within ~ 6 degrees for $r_p \gtrsim 0.3 \times (R_1 + R_2)$, where R_1 and R_2 are the radii of the colliding stars.
- 4. Change in Speed: In addition to the deflection angle, we consider the fractional change in speed, $\Delta v/v_{\infty}$, of the stars following a hit-and-run collision. For low-speed grazing collisions, tidal dissipation should be the main contributor to changes

in a star's speed. As r_p begins to decrease, shock dissipation should become the dominant means of slowing down the stars. We therefore fit $\Delta v/v_{\infty}$ using two terms, one representing the collision and one representing the tidal contribution. For large r_p , the latter term dominates. As r_p becomes small, the tidal term becomes negligable and the collision term begins to dominate. Section 4.4 details our approach and the final fitting formula. The formula is generally accurate to within a couple percent, with the exception of one data point near the capture boundary where $\Delta v/v_{\infty}$ is underpredicted by $\sim 10\%$.

5. ML Algorithms: We use our two-dimensional grid as a testing ground for two ML algorithms, kNN and a NN, which offer tantalizing prospects for modeling large datasets. We use classification to predict the number of stellar remnants in Section 5.1 and regression to predict continuous target variables like the $f_{\rm ML}$ in Section 5.2. We find that the NN outperforms our best kNN model in all respects. The NN classifier correctly predicted the collision outcome for the entire test dataset, while kNN struggled with data points that fell near decision boundaries, which separate one class of collision outcomes from the others. The NN also yielded lower MSEs and maximum absolute errors for all target variables, and both the NN and kNN had the largest absolute errors in their predictions near boundaries between collision outcome classes,

where target variables also have the largest variance. Lastly, we found the NN to be on par with and in some cases exceeding the accuracy of fitting formulae, which were expressly tailored for the SPH data at hand.

Fitting formulae and ML both have advantages for modeling datasets. Fitting formulae can provide insights into the physical laws and limits of a system. However, as the parameter space for the initial conditions expands, they can also become increasingly complex to formulate and cumbersome to implement. Our results highlight the promise of NNs to model collisions in complex environments, where the types of collisions are as diverse as the stellar and compact object populations that reside there.

We thank Tjitske Starkenburg and Enrico Ramirez-Ruiz for valuable discussion. S.C.R. thanks the CIERA Lindheimer Fellowship for support. Support for E.G.P. was provided by the National Science Foundation Graduate Research Fellowship Program under Grant DGE-2234667. F.K. acknowledges support from the CIERA Postdoctoral Fellowship. This research was also supported in part through the computational resources and staff contributions provided for the Quest high-performance computing facility at Northwestern University, which is jointly supported by the Office of the Provost, the Office for Research, and Northwestern University Information Technology.

REFERENCES

Agarap, A. F. 2018, arXiv e-prints, arXiv:1803.08375, doi: 10.48550/arXiv.1803.08375
Alexander, T. 1999, ApJ, 527, 835, doi: 10.1086/308129
Amaro Seoane, P. 2023, arXiv e-prints, arXiv:2302.00014, doi: 10.48550/arXiv.2302.00014
—. 2025, arXiv e-prints, arXiv:2509.12352, doi: 10.48550/arXiv.2509.12352
Ashkenazy, Y., & Balberg, S. 2024, arXiv e-prints, arXiv:2412.07491, doi: 10.48550/arXiv.2412.07491

Bailey, V. C., & Davies, M. B. 1999, MNRAS, 308, 257, doi: 10.1046/j.1365-8711.1999.02740.x

Balberg, S. 2024, ApJ, 962, 150, doi: 10.3847/1538-4357/ad1690

Balberg, S., Sari, R., & Loeb, A. 2013, MNRAS, 434, L26, doi: 10.1093/mnrasl/slt071

Balsara, D. S. 1995, Journal of Computational Physics, 121, 357, doi: 10.1016/S0021-9991(95)90221-X

Binney, J., & Tremaine, S. 2008, Galactic Dynamics: Second Edition

Brutman, Y., Steinberg, E., & Balberg, S. 2024, arXiv e-prints, arXiv:2408.16383,

doi: 10.48550/arXiv.2408.16383

Cover, T., & Hart, P. 1967, IEEE Transactions on Information Theory, 13, 21, doi: 10.1109/TIT.1967.1053964

Crespi, S., Ali-Dib, M., & Dobbs-Dixon, I. 2024, A&A, 685, A86, doi: 10.1051/0004-6361/202346519

Dale, J. E., & Davies, M. B. 2006, Monthly Notices of the Royal Astronomical Society, 366, 1424, doi: 10.1111/j.1365-2966.2005.09937.x

Dale, J. E., Davies, M. B., Church, R. P., & Freitag, M. 2009, MNRAS, 393, 1016,

doi: 10.1111/j.1365-2966.2008.14254.x

David, L. P., Durisen, R. H., & Cohn, H. N. 1987a, ApJ, 313, 556, doi: 10.1086/164997

- —. 1987b, ApJ, 316, 505, doi: 10.1086/165222
- Davies, M. B., Church, R. P., Malmberg, D., et al. 2011, in Astronomical Society of the Pacific Conference Series,
 Vol. 439, The Galactic Center: a Window to the Nuclear Environment of Disk Galaxies, ed. M. R. Morris, Q. D.
 Wang, & F. Yuan, 212. https://arxiv.org/abs/1002.0338
- Dessart, L., Ryu, T., Amaro Seoane, P., & Taylor, A. M. 2024, A&A, 682, A58, doi: 10.1051/0004-6361/202348228
- Duncan, M. J., & Shapiro, S. L. 1983, ApJ, 268, 565, doi: 10.1086/160980
- Fabian, A. C., Pringle, J. E., & Rees, M. J. 1975, MNRAS, 172, 15, doi: 10.1093/mnras/172.1.15P
- Ferrarese, L., & Ford, H. 2005, SSRv, 116, 523, doi: 10.1007/s11214-005-3947-6
- Freitag, M., & Benz, W. 2002, A&A, 394, 345, doi: 10.1051/0004-6361:20021142
- —. 2005, MNRAS, 358, 1133,doi: 10.1111/j.1365-2966.2005.08770.x
- Fukushima, K. 1969, IEEE Transactions on Systems Science and Cybernetics, 5, 322, doi: 10.1109/TSSC.1969.300225
- Gaburov, E., Lombardi, James C., J., & Portegies Zwart, S. 2010, MNRAS, 402, 105,
 - doi: 10.1111/j.1365-2966.2009.15900.x
- Gallego-Cano, E., Schödel, R., Dong, H., et al. 2018, A&A, 609, A26, doi: 10.1051/0004-6361/201730451
- Genzel, R., Eisenhauer, F., & Gillessen, S. 2010a, Reviews of Modern Physics, 82, 3121, doi: 10.1103/RevModPhys.82.3121
- —. 2010b, Reviews of Modern Physics, 82, 3121, doi: 10.1103/RevModPhys.82.3121
- Genzel, R., Schödel, R., Ott, T., et al. 2003, ApJ, 594, 812, doi: 10.1086/377127
- Ghez, A. M., Salim, S., Hornstein, S. D., et al. 2005, ApJ, 620, 744, doi: 10.1086/427175
- Ghez, A. M., Duchêne, G., Matthews, K., et al. 2003, ApJL, 586, L127, doi: 10.1086/374804
- Gibson, C. F. A., Kıroğlu, F., Lombardi, J. C., et al. 2025, ApJ, 980, 109, doi: 10.3847/1538-4357/ad9b80
- Glorot, X., Bordes, A., & Bengio, Y. 2011, in Proceedings of the Fourteenth International Conference on Artificial Intelligence and Statistics, 315–323
- Goldstein, J., & Townsend, R. H. D. 2020, ApJ, 899, 116, doi: 10.3847/1538-4357/aba748
- González, E., Kremer, K., Chatterjee, S., et al. 2021, ApJL, 908, L29, doi: 10.3847/2041-8213/abdf5b
- Hwang, J., Lombardi, J. C., J., Rasio, F. A., & Kalogera, V. 2015, ApJ, 806, 135, doi: 10.1088/0004-637X/806/1/135
- Kingma, D. P., & Ba, J. 2014, arXiv e-prints, arXiv:1412.6980, doi: 10.48550/arXiv.1412.6980

Kıroğlu, F., Lombardi, J. C., Kremer, K., et al. 2023, ApJ, 948, 89, doi: 10.3847/1538-4357/acc24c

- Kochanek, C. S. 1992, ApJ, 385, 604, doi: 10.1086/170966
- Lai, D., Rasio, F. A., & Shapiro, S. L. 1993, ApJ, 412, 593, doi: 10.1086/172946
- Lee, H. M., & Ostriker, J. P. 1986, ApJ, 310, 176, doi: 10.1086/164674
- Lombardi, J. C., J., Proulx, Z. F., Dooley, K. L., et al. 2006, ApJ, 640, 441, doi: 10.1086/499938
- Lombardi, James C., J., Warren, J. S., Rasio, F. A., Sills, A., & Warren, A. R. 2002, ApJ, 568, 939, doi: 10.1086/339060
- Lombardi, Jr., J. C., Rasio, F. A., & Shapiro, S. L. 1996, ApJ, 468, 797, doi: 10.1086/177736
- Loshchilov, I., & Hutter, F. 2017, arXiv e-prints, arXiv:1711.05101, doi: 10.48550/arXiv.1711.05101
- Maas, A. L., Hannun, A. Y., & Ng, A. Y. 2013, in Proc. ICML Workshop on Deep Learning for Audio, Speech and Language Processing
- Mardling, R. A., & Aarseth, S. J. 2001, MNRAS, 321, 398, doi: 10.1046/j.1365-8711.2001.03974.x
- Mastrobuono-Battisti, A., Church, R. P., & Davies, M. B. 2021, MNRAS, 505, 3314, doi: 10.1093/mnras/stab1409
- Monaghan, J. J. 2002, MNRAS, 335, 843, doi: 10.1046/j.1365-8711.2002.05678.x
- Murphy, B. W., Cohn, H. N., & Durisen, R. H. 1991, ApJ, 370, 60, doi: 10.1086/169793
- Nandez, J. L. A., Ivanova, N., & Lombardi, Jr., J. C. 2014, ApJ, 786, 39, doi: 10.1088/0004-637X/786/1/39
- Neumayer, N., Seth, A., & Böker, T. 2020, A&A Rv, 28, 4, doi: 10.1007/s00159-020-00125-0
- Press, W. H., & Teukolsky, S. A. 1977, ApJ, 213, 183, doi: 10.1086/155143
- Price, D. J., & Monaghan, J. J. 2007, MNRAS, 374, 1347, doi: 10.1111/j.1365-2966.2006.11241.x
- Rasio, F. A. 1991, PhD thesis, Cornell University, New York Rauch, K. P. 1999, ApJ, 514, 725, doi: 10.1086/306953
- Ray, A., Kembhavi, A. K., & Antia, H. M. 1987, A&A, 184, 164
- Robbins, H., & Monro, S. 1951, The Annals of Mathematical Statistics, 22, 400, doi: 10.1214/aoms/1177729586
- Rodriguez, C. L., Weatherford, N. C., Coughlin, S. C., et al. 2022, ApJS, 258, 22, doi: 10.3847/1538-4365/ac2edf
- Rose, S. C., & MacLeod, M. 2024, ApJL, 963, L17, doi: 10.3847/2041-8213/ad251f
- Rose, S. C., & Mockler, B. 2025, ApJL, 985, L40, doi: 10.3847/2041-8213/add266
- Rose, S. C., Naoz, S., Sari, R., & Linial, I. 2022, ApJL, 929, L22, doi: 10.3847/2041-8213/ac6426

- 2023, arXiv e-prints, arXiv:2304.10569, doi: 10.48550/arXiv.2304.10569
- Rubin, D., & Loeb, A. 2011, Advances in Astronomy, 2011, 174105, doi: 10.1155/2011/174105
- Rumelhart, D. E., Hinton, G. E., & Williams, R. J. 1986, Nature, 323, 533, doi: 10.1038/323533a0
- Ryu, T., Amaro Seoane, P., Taylor, A. M., & Ohlmann,
 S. T. 2024, MNRAS, 528, 6193,
 doi: 10.1093/mnras/stae396
- Schödel, R., Genzel, R., Ott, T., & Eckart, A. 2003, Astronomische Nachrichten Supplement, 324, 535, doi: 10.1002/asna.200385048
- Sills, A., Faber, J. A., Lombardi, James C., J., Rasio, F. A., & Warren, A. R. 2001, ApJ, 548, 323, doi: 10.1086/318689
- Sills, A., Lombardi, James C., J., Bailyn, C. D., et al. 1997, ApJ, 487, 290, doi: 10.1086/304588

- Springel, V., & Hernquist, L. 2002, MNRAS, 333, 649, doi: 10.1046/j.1365-8711.2002.05445.x
- Sun, M., Townsend, R. H. D., & Guo, Z. 2023, ApJ, 945, 43, doi: 10.3847/1538-4357/acb33a
- Townsend, R. H. D., Goldstein, J., & Zweibel, E. G. 2018, MNRAS, 475, 879, doi: 10.1093/mnras/stx3142
- Townsend, R. H. D., & Teitler, S. A. 2013, MNRAS, 435, 3406, doi: 10.1093/mnras/stt1533
- Wendland, H. 1995, Advances in Computational Mathematics, 4, 389, doi: 10.1007/BF02123482
- Winter, P. M., Burger, C., Lehner, S., et al. 2023, MNRAS, 520, 1224, doi: 10.1093/mnras/stac2933
- Yu, Q., & Tremaine, S. 2003, ApJ, 599, 1129, doi: 10.1086/379546